



HAL
open science

Dehydration-induced instabilities at intermediate depths in subduction zones

Nicolas Brantut, Ioannis Stefanou, Jean Sulem

► **To cite this version:**

Nicolas Brantut, Ioannis Stefanou, Jean Sulem. Dehydration-induced instabilities at intermediate depths in subduction zones. *Journal of Geophysical Research: Solid Earth*, 2017, 10.1002/2017JB014357. hal-01568176

HAL Id: hal-01568176

<https://enpc.hal.science/hal-01568176>

Submitted on 24 Jul 2017

HAL is a multi-disciplinary open access archive for the deposit and dissemination of scientific research documents, whether they are published or not. The documents may come from teaching and research institutions in France or abroad, or from public or private research centers.

L'archive ouverte pluridisciplinaire **HAL**, est destinée au dépôt et à la diffusion de documents scientifiques de niveau recherche, publiés ou non, émanant des établissements d'enseignement et de recherche français ou étrangers, des laboratoires publics ou privés.

¹ Dehydration-induced instabilities at intermediate ² depths in subduction zones

Nicolas Brantut¹, Ioannis Stefanou² and Jean Sulem²

N. Brantut, Department of Earth Science, University College London, Gower Street, London WC1E 6BT, UK. (n.brantut@ucl.ac.uk)

¹Rock and Ice Physics Laboratory and Seismological Laboratory, Department of Earth Sciences, University College London, London, UK.

²Université Paris-Est, Laboratoire Navier, CNRS UMR 8205, École des Ponts – ParisTech, France.

3 **Abstract.** We formulate a model for coupled deformation and dehydra-
4 tion of antigorite, based on a porosity-dependent yield criterion and includ-
5 ing shear enhanced compaction. A pore pressure and compaction instabil-
6 ity can develop when the net volume change associated with the reaction is
7 negative, i.e., at intermediate-depth in subduction zones. The instability cri-
8 terion is derived in terms of the dependence of the yield criterion on poros-
9 ity: if that dependence is strong, instabilities are more likely to occur. We
10 also find that the instability is associated with strain localisation, over char-
11 acteristic length scales determined by the hydraulic diffusivity, the elasto-
12 plastic parameters of the rock, and the reaction rate. Typical lower bounds
13 for the localisation length are of the order of 10 to 100 m for antigorite de-
14 hydration and deformation at 3 GPa. The fluid pressure and deformation in-
15 stability is expected to induce stress build-up in the surrounding rocks form-
16 ing the subducted slab, which provides a mechanism for the nucleation and
17 propagation of intermediate-depth earthquakes.

1. Introduction

18 During prograde metamorphism in subduction zones, hydrous phases such as serpentines
19 progressively dehydrate, forming free fluid phases at depth. Such dehydration reactions are
20 systematically associated with a net decrease in solid volume (the reactions forming solid
21 products denser than reactants), and with a variable change in fluid volume, the sign of
22 which being controlled by the pressure and temperature conditions at which the reaction
23 occurs. From initially nonporous metamorphic rocks (such as antigorite serpentinite),
24 dehydration reactions therefore produce, at least transiently, a porous rock saturated
25 with fluids, the rheology of which is markedly different from the original rock [e.g. *Rutter*
26 *et al.*, 2009]. The occurrence of metamorphic dehydration reactions has therefore a great
27 impact on the stress/strain state in subduction zones.

28 One key specific impact of dehydration reactions is their potential to trigger unstable
29 faulting and earthquakes, a phenomenon generally termed “dehydration embrittlement”.
30 This phenomenon corresponds to the transition from ductile to brittle deformation due to
31 a dehydration-induced increase in pore fluid pressure. It is often thought that dehydration-
32 embrittlement is one of the main causes of, or is at least linked to, intermediate-depth
33 earthquakes in subduction zones [e.g., *Hacker et al.*, 2003b]. Dehydration embrittlement
34 has been observed experimentally [e.g., *Raleigh and Paterson*, 1965; *Murrell and Ismail*,
35 1976] and is well explained theoretically when the reaction produces an excess fluid vol-
36 ume, i.e., typically at relatively low pressure conditions (e.g., less than around 2.5 GPa
37 in antigorite). Under those conditions, the excess fluid volume generated by the reac-
38 tion tends to increase the pore fluid pressure, reducing the effective stress, and therefore

39 bringing back the material into the brittle field. At higher pressure, where the total vol-
40 ume change of the dehydration reaction is negative, laboratory experiments indicate that
41 dehydration embrittlement and earthquake instability might still occur [e.g. *Jung et al.*,
42 2004], but the exact mechanism remains unclear. One possibility is that the reaction
43 products are plastically weak and facilitate brittle deformation in their surroundings [e.g.
44 *Rutter et al.*, 2009; *Brantut and Sulem*, 2012]. Another potential mechanism is that the
45 porosity generated by the reaction is rapidly compacted, hence producing a pore pressure
46 rise which could bring back the material into the brittle regime.

47 Coupling between mechanical compaction and dehydration reactions has been inves-
48 tigated in detail in the case of viscous rock rheology: in his seminal study, *Connolly*
49 [1997] (followed by *Connolly and Podladchikov* [1998] and *Connolly and Podladchikov*
50 [2004], summarised recently in *Connolly* [2004]) used a viscous compaction rheology cou-
51 pled to devolatilisation reactions together with a power-law relation between porosity
52 and permeability, and determined that compaction would drive pore fluid pressure up to
53 near-lithostatic values, while producing intermittent upward motions of fluid (so-called
54 porosity-waves). Despite the great success of this model for the prediction of fluid extrac-
55 tion from the lower crust (or along subduction zones, see *Skarbek and Rempel* [2016]), one
56 key assumption is that the compaction behaviour is essentially driven by a viscous creep
57 process, and does not include the instantaneous response of the material.

58 Serpentinites, and more specifically the high pressure form, antigorite, are known to
59 behave in a semi-brittle manner even at high pressure and temperature [e.g. *Chernak*
60 *and Hirth*, 2010; *Proctor and Hirth*, 2016], i.e., antigorite deformation systematically in-
61 volves a significant degree of microcracking, and its behaviour at high pressure is similar

62 to cataclastic flow. Furthermore, laboratory experiments [*Rutter et al.*, 2009] show that
63 dehydrated and partially dehydrated serpentinite behave essentially like classical porous
64 rocks, and that concepts of porous rock mechanics can be used to describe their me-
65 chanical behaviour. Therefore, a purely viscous constitutive law may not capture all the
66 features and potential instabilities associated with coupled compaction and dehydration
67 in antigorite.

68 Here, we model coupled dehydration and deformation in antigorite using as a first
69 approximation a time-independent inelastic flow law which includes strain hardening,
70 strain-dependent dilatancy/compaction and a porosity-dependent yield envelope. Our
71 approach is based on the concepts typically used to model the behaviour of porous rocks
72 [e.g. *Rudnicki and Rice*, 1975; *Issen and Rudnicki*, 2000; *Wong and Baud*, 2012; *Stefanou*
73 *and Sulem*, 2014], and dehydration has here an indirect effect by contributing to the
74 overall change in porosity and fluid pressure. In this framework, two types of instabilities
75 can arise: a rate-independent bifurcation related to the constitutive behaviour of the rock,
76 and a reaction-driven, rate-dependent instability due to the growth to small pore pressure
77 perturbations. We specifically focus on the behaviour of serpentinite under conditions
78 such that the dehydration reaction produces a negative total volume change, with the
79 aim of determining whether pore pressure instabilities can occur.

2. Model and governing equations

2.1. Fluid mass balance and pore pressure change

80 During dehydration, antigorite becomes a porous aggregate, with a porosity n filled
81 with water at a pressure denoted p_f . We consider that the porosity of the aggregate is
82 connected (at least at the scale of interest, here of the order of 10 to 100 metres), and that

83 the fluid flows through the rock according to Darcy's law with a permeability k . The fluid
 84 pressure is modified by two independent contributions: the elasto-plastic compaction of
 85 the rock (bulk volumetric strain ϵ , taken negative in compression), and the generation of
 86 fluids from the dehydration reaction. These assumptions lead to the following governing
 87 equation for pore pressure (see full derivation in Appendix A1):

$$\frac{\partial p_f}{\partial t} = \frac{k}{\eta c_b} \nabla^2 p_f - \frac{1}{c_b} \frac{\partial \epsilon}{\partial t} + \frac{m_d^0 (1 + \rho_f \Delta_r V_s)}{\rho_f c_b} \frac{\partial \xi}{\partial t}, \quad (1)$$

88 where m_d^0 is the total fluid mass that can be released by the reaction per unit rock volume,
 89 ρ_f is the fluid density, $\Delta_r V_s$ is the solid volume change of the reaction, $\partial \xi / \partial t$ is the reaction
 90 rate, and

$$c_b = (1 - n)c_s + nc_f \quad (2)$$

91 is an effective compressibility combining the compressibility of the solid c_s , the compress-
 92 ibility of the fluid c_f , and the porosity n . Note here that c_b is *not* the usual storage
 93 capacity, because we did not split the volumetric strain rate into an elastic and plastic
 94 one.

2.2. Rheology

95 It is well established experimentally that antigorite aggregates undergo a brittle to duc-
 96 tile transition at confining pressures of the order of 300 to 400 MPa [*Escartín et al.*, 1997],
 97 and that this transition depends weakly on temperature (within antigorite's stability field).
 98 Near the dehydration temperature of antigorite, the ductile behaviour remains dominated
 99 by cataclastic flow even at mantle pressures [*Chernak and Hirth*, 2010; *Proctor and Hirth*,
 100 2016], which is most likely due to the strong [001] cleavage plane and the insufficient num-
 101 ber of independent slip systems in antigorite single crystals. Across the stability boundary

102 of antigorite, a very significant volume change occurs: the solid volume tends to decrease
103 by up to around 25%, generating a porosity occupied by pressurised water. Therefore,
104 at pressure and temperature conditions near its stability boundary, antigorite is expected
105 to behave very much like a ductile (cataclastic) porous rock. Such a behaviour has been
106 well documented in lizardite by *Rutter et al.* [2009], and we assume here that the same
107 behaviour applies to antigorite.

108 In order to describe the elasto-plastic behaviour of antigorite, we introduce the yield
109 function $f(\sigma, \zeta)$, where σ is the stress tensor (here we follow the sign convention of con-
110 tinuum mechanics and take compressive stresses as negative) and ζ is an internal variable
111 on which the yield cap depends. The yield function limits the elastic domain in the stress
112 space ($f < 0$, see Figure 1). It is assumed that inelastic strain increments are generated
113 when the stress state lies on the yield surface ($f = 0$) and if loading is taking place. ζ
114 can be identified to either the porosity of the material, or more directly to the reaction
115 progress in the case of a pure chemical control over the material's strength [*Stefanou and*
116 *Sulem, 2014; Sulem and Stefanou, 2016*]. While either option could be deemed acceptable
117 in the light of the available experimental data from *Rutter et al.* [2009], we will develop
118 our model assuming that the primary control on the rock's strength is given by its poros-
119 ity (a robust observation in porous rocks, see *Wong and Baud* [2012]). We therefore
120 equate incremental changes in the internal variable ζ to irreversible (inelastic) porosity
121 changes. We also assume, in accordance with experimental observations, that the material
122 undergoes strain hardening. The incremental constitutive behaviour resulting from our

assumptions is written as follows (see full derivation in Appendix A2):

$$dp' = \frac{GK [(1 + (h - f'\beta)/G)d\epsilon - \beta d\gamma]}{h - f'\beta + G + \beta\mu K} + \frac{f'\beta K m_d^0 \Delta_r V_s}{h - f'\beta + G + \beta\mu K} d\xi, \quad (3)$$

$$d\tau = \frac{GK [-\mu d\epsilon + ((h - f'\beta)/K + \beta\mu)d\gamma]}{h - f'\beta + G + \beta\mu K} + \frac{f'G m_d^0 \Delta_r V_s}{h - f'\beta + G + \beta\mu K} d\xi, \quad (4)$$

where p' is the Terzaghi effective mean stress ($p' = p + p_f$, where p is the mean stress), τ is the shear stress (taken equal to the square root of the second invariant of the deviatoric stress tensor), K and G are the bulk and shear elastic moduli of the rock, respectively, γ is the shear strain (taken equal to the square root of the second invariant of the deviatoric strain tensor), h is the strain hardening coefficient, β is the dilatancy factor and $f' = \partial f / \partial \zeta$ is the dependency of the yield cap on porosity. We observe in equations 3 and 4 that the effect of the variation of f with porosity (terms in f') on the mechanical behaviour is entirely captured by the modified hardening modulus $h - f'\beta$. The chemical coupling appears through the product $f'\Delta_r V_s$: the reaction has only an indirect effect, which is to modify the porosity. The solid volume change is always negative (porosity creation), and f' is positive (the yield surface shrinks with increasing porosity), so that the overall effect of the reaction is to weaken the material.

2.3. Reaction rate

A very general formulation of mineral reaction rates is given by [Lasaga and Rye, 1993]

$$\frac{\partial \xi}{\partial t} = \kappa A_{\text{rlm}} s |\Delta G|^{n_r}, \quad (5)$$

where κ is the temperature-dependent kinetic constant (typically following an Arrhenius law), A_{rlm} is the specific surface area of the rate-limiting mineral, ΔG is the Gibbs energy change of the reaction, s is the opposite of the sign of ΔG , and n_r is the order of the reaction. Under isothermal conditions, and for small departures from equilibrium, we can

141 expand ΔG in terms of pore pressure; only retaining the leading order term, we have
 142 [*Wang and Wong, 2003*]

$$\Delta G \approx c'(p_f - p_{\text{eq}}), \quad (6)$$

143 where $c' = \partial\Delta G/\partial p_f$ and p_{eq} is the pore pressure at equilibrium. Following *Wang and*
 144 *Wong [2003]*, we can rewrite 5 as

$$\frac{\partial\xi}{\partial t} = sr_0 \frac{A_{\text{rlm}}}{A_{\text{rlm}}^0} |1 - p_f/p_{\text{eq}}|^{n_r}, \quad (7)$$

145 where r_0 is a reference reaction rate, and A_{rlm}^0 is the surface area of the rate limiting
 146 mineral at the reference rate. The change in surface area is not very well constrained
 147 by experimental data. Hence, for simplicity, in the following we will consider the ratio
 148 $A_{\text{rlm}}/A_{\text{rlm}}^0 \approx 1$. This simplification is valid only when the reaction progress is small, i.e.,
 149 when depletion of the reaction is negligible ($\xi \ll 1$).

2.4. Geometry and stress equilibrium

150 We consider a simple system made of a uniform horizontal layer of antigorite, sufficiently
 151 extended so that lateral strains can be neglected (i.e., the system is invariant in the plane
 152 of the layer). In this geometry, the vertical stress is given by $p - 2\tau/\sqrt{3}$, and stress
 153 equilibrium requires that:

$$\frac{\partial}{\partial y} \left(p - \frac{2}{\sqrt{3}}\tau \right) = 0. \quad (8)$$

154 where y denotes the vertical coordinate. The boundary condition is a constant applied
 155 vertical stress, which implies that

$$\frac{\partial p}{\partial t} - \frac{2}{\sqrt{3}} \frac{\partial \tau}{\partial t} = 0. \quad (9)$$

156 In such a geometry, only the vertical strain component is nonzero. Because no lateral
 157 deformation is allowed, the vertical strain is equal to the volumetric strain. Therefore,

158 the shear and volumetric strains are related to one another by:

$$\gamma + \frac{2}{\sqrt{3}}\epsilon = 0. \quad (10)$$

159 Using relations (9) and (10) in the incremental constitutive formulation (Equations 3,
160 4), and combining with the fluid mass conservation (Equation 1) and expression (7) for
161 the reaction rate, we arrive at a single, nonlinear diffusion equation that governs the fluid
162 pressure (see details in Appendix A3):

$$\frac{\partial p_f}{\partial t} = \frac{Mk/\eta}{1 + c_b M} \frac{\partial^2 p_f}{\partial y^2} + \frac{Mm_d^0(1/\rho_f + \Delta_r V_s) - f'X}{1 + c_b M} sr_0 \left| 1 - \frac{p_f}{p_{eq}} \right|^{n_r}, \quad (11)$$

163 where

$$M = \frac{GK}{h - f'\beta + G + \beta\mu K} \left[\left(1 + \frac{2}{\sqrt{3}}\mu \right) \left(1 + \frac{2}{\sqrt{3}}\beta \right) + (h - f'\beta) \left(\frac{1}{G} + \frac{4}{3K} \right) \right], \quad (12)$$

164 and

$$X = -m_d^0 \Delta_r V_s \frac{\beta K - 2G/\sqrt{3}}{h - f'\beta + G + \beta\mu K}. \quad (13)$$

3. Parameters

3.1. Yield function

The model described above contains a number of parameters that ought to be constrained from experimental data. The yield cap can be constrained from the extensive dataset of *Rutter et al.* [2009] on intact and dehydrated blocks of lizardite. The data used are shown in Figure 2. For simplicity, we use a modified Cam-clay yield surface, given by

$$f(p', \tau) = \tau - C\sqrt{(b + p')(p^* - p')} = 0, \quad (14)$$

165 where C is the critical state line ratio, b is the tensile strength, and p^* is the compaction
166 yield pressure (following the notation of *Wong and Baud* [2012]). Specific values of C , b
167 and p^* for intact, partially and fully dehydrated serpentinites are reported in Figure 2.

168 In accordance with observations on porous sandstones, the critical compaction pressure
169 p^* decreases with increasing porosity. *Zhang et al.* [1990] proposed a grain crushing model
170 in which p^* scales with the porosity n as $p^* \propto n^{-3/2}$. For the serpentinite samples
171 dehydrated at 35 MPa effective pressure and deformed at room temperature (squares
172 in Figure 2), we find a reasonable fit with $p^* = 130$ MPa, while the inferred porosity of
173 the sample was around 19%. The partially dehydrated samples (diamonds in Figure 2)
174 had a porosity of around 4%, and we determine a p^* of 380 MPa. The relationship between
175 p^* and n for these two sample types does not seem compatible with the scaling proposed
176 by *Zhang et al.* [1990]. Here we will use an empirical scaling $p^* \propto 1/n$ [*Rutter and Glover,*
177 2012], with a constant of proportionality equal to 19 MPa. The corresponding yield caps
178 are reported as dotted lines in Figure 2.

179 Obviously, the yield cap described by Equation 14 is not appropriate as the porosity
180 approaches zero, since in that case p^* diverges. However, the focus of this work is the
181 description of rocks that are already undergoing dehydration, i.e., in which the porosity is
182 never exactly zero. Furthermore, in absence of a more complete dataset on dehydrated and
183 partially dehydrated serpentinite, the Cam-clay yield surface is one of the simplest yield
184 criterion which is closed at high pressure (i.e., the material can fail by pure hydrostatic
185 compaction). Hence, our choice for the yield function should be viewed as a first order
186 approximation which incorporates the essential qualitative elements of the behaviour of
187 dehydrating serpentinite: a yield cap that is closed at high pressure and that shrinks with
188 increasing porosity.

3.2. Mechanical and hydraulic parameters

189 The elastic properties of serpentinite can be obtained from Voigt-Reuss-Hill averages
 190 of the single crystal properties, and are given by *Bezacier et al.* [2010]: $K = 67.9$ GPa,
 191 $G = 38.5$ GPa. The average Poisson's ratio is hence $\nu = 0.26$. Note that we are modelling
 192 dehydrating serpentinite, and hence the average elastic properties of the rock should be
 193 made dependent upon the evolving rock mineralogical composition and porosity. However,
 194 we focus here on the initiation of the dehydration reaction, and hence expect that the
 195 pure antigorite end-member is a good approximation to the overall properties of the rock
 196 at the beginning of dehydration.

The friction coefficient μ is given by the local slope of the yield envelope (equation A24):

$$\mu = \frac{\partial f}{\partial p'} = C \frac{2p' + b - p^*}{2\sqrt{(p' + b)(p^* - p')}}. \quad (15)$$

197 In the framework of associated plasticity, we could assume that the dilatancy factor is
 198 merely equal to the friction coefficient. However, it is well known that rocks do not follow
 199 associated flow rules, and hence we shall leave the dilatancy factor β as a free parameter,
 200 and explore how it influences the stability of compaction in our model. Likewise, we
 201 will leave the hardening coefficient as a free parameter, in order to encompass the widest
 202 possible range of behaviours.

203 The permeability of the rock is expected to vary as a function of porosity, and hence
 204 be impacted by the compaction of the rock. However, these second order controls on
 205 permeability should only influence the behaviour of the material at large times, and not
 206 the initiation of the instability. For instance, using power-law permeability-porosity re-
 207 lationships, *Connolly* [1997] has shown that a dehydrating rock can generate travelling
 208 porosity pulses, a well known feature of nonlinear parabolic equations. Since we want

209 to focus on the initiation of the instability, we shall assume a constant value for the
210 permeability, keeping in mind that this assumption should be relaxed when modelling
211 the long-term evolution of the system. The permeability of dehydrating serpentinite was
212 measured by *Tenthorey and Cox* [2003], who report $k = 10^{-22}$ m² for the intact material
213 and $k = 10^{-20}$ to 10^{-18} m² during dehydration at 600°C and 700°C, respectively. Here
214 we choose $k = 10^{-20}$ m² as a representative value for serpentinites which are dehydrating
215 not far from equilibrium.

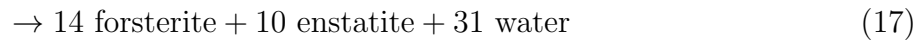
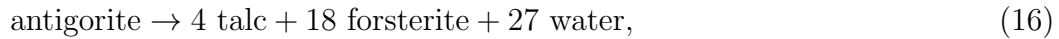
216 The viscosity of the fluid η can be precisely determined from interpolation of experimen-
217 tal measurements. We will use here the formulation of the International Association for
218 the Properties of Water and Steam, 2008 (<http://iapws.org/relguide/visc.pdf>), and com-
219 pute the appropriate viscosity at the target pressure and temperature conditions. The
220 resulting viscosity of water ranges from $\eta = 6.9 \times 10^{-5}$ to 4.9×10^{-7} Pa s at $p_f = 2$ GPa
221 and 600°C and $p_f = 5$ GPa and 700°C, respectively.

222 The effective compressibility of the rock, c_b , does not play any role in the stability of
223 the system; it is only required for the computation of the full numerical solutions, and
224 acts as a scaling factor for the pore pressure rate. Here we compute c_b from Equation (2),
225 assuming that $c_s = 1/K$.

3.3. Chemical parameters

The parameters associated with the chemical reaction can be obtained from the ther-
modynamic properties of the mineral (and fluid) involved. At elevated pressure and

temperature, there are three distinct dehydration reactions involving antigorite:



226 The properties of each mineral can be extracted from thermodynamic tables [e.g. *Holland*
 227 *and Powell*, 1998; *Hacker et al.*, 2003a], and are reported in Table 1. The thermodynamic
 228 properties of water are determined as a function of pressure and temperature from the
 229 IAPWS formulation 95.

230 The computation of the solid volume change $\Delta_r V_s$ requires the knowledge of the molar
 231 volumes of each solid phase at the pressure and temperature conditions of each reaction.
 232 The molar volumes are computed following the approach explained in *Hacker et al.* [2003a],
 233 which is recalled in Appendix B for completeness.

234 The phase boundaries and net volume change of each reaction (16, 17, 18) are shown as
 235 a function of pressure and temperature in Figure 3. Average volume changes along each
 236 phase boundary are presented in Table 2.

237 In addition, the knowledge of the molar volume of antigorite allows to compute precisely
 238 the total potential mass of water releasable by each reaction, m_d^0 . Because antigorite is not
 239 very compressible, the main factor influencing m_d^0 is the stoichiometry of the reactions.
 240 The computed averages of m_d^0 for each reaction are shown in Table 2.

241 The reaction kinetics of antigorite as a function of pressure is not well constrained by
 242 existing experimental data, which typically focus on the effect of temperature. However,
 243 the formulation 5 is general, and hence kinetic parameters obtained from experiments in
 244 which ΔG is imposed from a temperature over- or under-step should also be valid in the

245 case when ΔG changes due to pressure fluctuations. Here we extract kinetic parameters
 246 from the study of *Eggler and Ehmman* [2010], in which the dehydration kinetics of antig-
 247 orite was determined at 2 GPa (i.e., for reaction 17) as a function of temperature. At a
 248 temperature T , the rate of antigorite dehydration is given as

$$\text{rate} = \kappa' A_{\text{rlms}} \left| \frac{\Delta G}{RT} \right|^{n_r} \quad \text{in mol}_{\text{atg}}/\text{cm}_{\text{rock}}^3/\text{s}, \quad (19)$$

249 where R is the gas constant. In terms of reaction progress ξ , we rewrite equation 19 as

$$\frac{\partial \xi}{\partial t} = s r_0 \frac{A_{\text{rlms}}}{A_{\text{rlms}}^0} |1 - p_f/p_{\text{eq}}|^{n_r}, \quad (20)$$

250 where

$$r_0 = V_m A_{\text{rlms}}^0 \kappa' \left| \frac{p_{\text{eq}} c'}{RT} \right|^{n_r}. \quad (21)$$

251 The molar volume of antigorite V_m can be taken as the average along the phase boundary
 252 between antigorite and forsterite, enstatite and water, using equation B6. This yields
 253 $V_m \approx 1.73 \times 10^{-3} \text{ m}^3/\text{mol}_{\text{atg}}$. The initial specific surface area of antigorite, A_{rlms}^0 , depends
 254 on the grain size and shape; for square prisms with width W and length L , $A_{\text{rlms}}^0 =$
 255 $(2W^2 + 4LW)/LW^2$. Using $W = 50 \text{ }\mu\text{m}$ and $L = 10 \text{ }\mu\text{m}$, we find $A_{\text{rlms}}^0 = 2.8 \times 10^5 \text{ m}^2/\text{m}^3$.
 256 The rate constant κ' given by *Eggler and Ehmman* [2010] is $9.2 \times 10^{-11} \text{ mol}_{\text{atg}}/\text{m}^2/\text{s}$. The
 257 coefficient c' , as defined in equation 6, is the net volume change of the reaction per unit
 258 mole of antigorite:

$$c' = \nu_f M_f (1/\rho_f + \Delta_r V_s). \quad (22)$$

259 Using the parameter value reported in Table 2 for the reaction of antigorite into forsterite
 260 and enstatite, we obtain $c' \approx 8.1 \times 10^{-5} \text{ m}^3/\text{mol}_{\text{atg}}$. The equilibrium pressure p_{eq} and the
 261 appropriate temperature T can be found from the phase boundary (see Figure 3). As a
 262 representative value, we choose $p_{\text{eq}} = 3 \text{ GPa}$ and $T \approx 640^\circ\text{C}$. Finally, *Eggler and Ehmman*

[2010] report that the exponent n_r is equal to one, i.e., the kinetic is linear. Combining all the above parameters into our lumped kinetic parameter r_0 , we find a representative value of

$$r_0 \approx 1.47 \times 10^{-6}/s. \quad (23)$$

4. Stability analysis

The system governed by Equation (11) involves two coupled phenomena: mechanical deformation (compaction), through the parameter M , and metamorphic effects with fluid production and porosity creation through the source term in (11). In this Section, we detail the possible sources of mechanical and chemical instabilities, and derive the key stability conditions in terms of the model parameters.

4.1. Mechanical instability

If $M < 0$, we immediately observe that Equation 11 is a diffusion equation with a negative diffusivity. This corresponds to an unstable system as non uniformities become more localised rather than more diffuse with increasing time. In fact, the condition $M < 0$ is strictly equivalent to the compaction localisation condition derived by *Issen and Rudnicki* [2000, their equation 19] for axisymmetric compression:

$$\frac{h - f'\beta}{G} < \frac{h_{\text{crit}}}{G} = -\frac{3K}{3K + 4G} \left(1 + \frac{2}{\sqrt{3}}\mu\right) \left(1 + \frac{2}{\sqrt{3}}\beta\right), \quad (24)$$

with the additional term $-f'\beta$ occurring here due to the explicit dependence of the yield cap on porosity. For a yield cap shrinking with increasing porosity, as expected and observed in dehydrating serpentinites (Figure 2), f' is positive, and β is negative (due to shear-enhanced compaction at high pressure). Hence, the critical hardening modulus is reduced when the yield cap is assumed to be directly dependent on porosity; this merely

reflects that the yield cap expansion due to shear hardening is in fact offset by a further yield cap expansion (resp. shrinkage) due to shear-induced compaction (resp. dilatancy).

Note, in passing, that we have derived here a slightly more general case for the compaction instability including pore fluid pressurisation effects; the stability condition, without chemical effects, is in fact $M/(1 + c_b M) < 0$. This has no practical consequence on the criterion because c_b is usually very small.

4.2. Chemical instability and overpressure development

The case of interest here is when $M > 0$ (Equation (12)), i.e., a mechanically stable case. Equation 11 is a nonlinear diffusion equation. We examine here the case when the total volume change of the reaction is negative, for which the reaction kinetics increases when p_f increases beyond p_{eq} . Before delving into the full analysis including the effect of pore pressure diffusion, it is instructive to first analyse the undrained case; the governing equation for pore pressure reduces to

$$\frac{\partial p_f}{\partial t} = \frac{M m_d^0 (1/\rho_f + \Delta_r V_s) - f' X}{1 + c_b M} r_0 \left(\frac{p_f}{p_{\text{eq}}} - 1 \right)^{n_r}. \quad (25)$$

Assuming constant parameters, this equation has an analytical solution, which is

$$p_f(t) = p_{\text{eq}} + (p_f^0 - p_{\text{eq}}) \exp \left(\frac{M m_d^0 (1/\rho_f + \Delta_r V_s) - f' X}{p_{\text{eq}} (1 + c_b M)} r_0 t \right) \quad (26)$$

if $n_r = 1$, and

$$p_f(t) = p_{\text{eq}} + \left(p_{\text{eq}}^{-n_r} (1 - n_r) r_0 \frac{M m_d^0 (1/\rho_f + \Delta_r V_s) - f' X}{1 + c_b M} t + (p_f^0 - p_{\text{eq}})^{1-n_r} \right)^{1/(1-n_r)} \quad (27)$$

if $n_r > 1$, where p_f^0 is the initial pore pressure in the system (a small perturbation above the equilibrium pressure).

297 In both cases (linear and nonlinear kinetics), the evolution of pore pressure is an un-
 298 bounded growth if

$$Mm_d^0(1/\rho_f + \Delta_r V_s) - f'X > 0. \quad (28)$$

299 For linear kinetics, the growth is exponential, while for nonlinear kinetics the growth
 300 corresponds to a finite time blow-up. In practice, this distinction is unimportant since
 301 pore pressure diffusion, as well as other nonlinearities not accounted for in our simplified
 302 system (such as the depletion of the reactant or the change in mechanical properties with
 303 the evolving deformation and mineralogy of the rock), are expected to strongly change
 304 the evolution of pore pressure at large times. Despite these subtleties, the solution of
 305 the undrained problem yields a key condition (Inequality 28) to observe a potential pore
 306 pressure runaway. This condition for instability can be expressed as a pair of conditions
 307 in terms of the dilatancy factor β and the dependence of the yield cap on porosity f' (see
 308 Appendix C1 for details):

$$\beta < \beta_{\text{crit}} = -(\sqrt{3}/2) \left(\frac{3}{2} \frac{1-\nu}{1-2\nu} \frac{1}{\rho_f \Delta_r V_s} + 1 \right)^{-1}, \quad (29)$$

$$f' > f'_{\text{crit}} = \sqrt{3} \frac{1-\nu}{1-2\nu} \frac{h - h_{\text{crit}}}{1 - \beta/\beta_{\text{crit}}} \left(1 + \frac{1}{\rho_f \Delta_r V_s} \right). \quad (30)$$

309 Using the numerical values detailed in the previous section, we remark that β_{crit} is always
 310 positive. Hence, for the cases of interest where $\beta < 0$ (shear enhanced compaction), we
 311 always have $\beta < \beta_{\text{crit}}$, and thus the condition for instability is simply $f' > f'_{\text{crit}}$.

312 The stability boundaries ($h = h_{\text{crit}} + f'\beta$ and $f' = f'_{\text{crit}}$) are shown as function of f'/G
 313 and β in Figure 4, where we have assumed $\beta = \mu$. For $h > 0$, the mechanical compaction
 314 bifurcation arises only for negative values of f' , while the reaction-driven compaction
 315 and pore pressure instability occurs only for positive values of f' , leaving an area of

316 stability between these two boundaries. For $h = 0$ (which seems relatively plausible for
 317 antigorite, see *Escartín et al.* [1997]), the stability boundaries do not overlap; the area of
 318 stability expands with decreasing (negative) values of β . Because the friction coefficient
 319 μ only appears in the expression for h_{crit} , changing μ independently from β (which is a
 320 reasonable choice for most rocks) has a moderate impact on the stability diagram for the
 321 pore pressure instability (condition (30)), but introduces large changes for the bifurcation
 322 criterion (condition (24)).

323 Using our assumed form for the yield function f , we note that f' diverges as porosity
 324 decreases towards zero: in practice, f' is potentially very large at the initiation of the
 325 dehydration reaction (when porosity is very low). If the applied stress is such that $\beta < 0$,
 326 as in the case at high effective pressure, then the reaction-driven instability is very probable
 327 at the onset of dehydration. This implies that the pore fluid pressure will quickly rise
 328 to decrease the effective stress; the pressure (solid and fluid) will hence equilibrate very
 329 suddenly, generating a transient pore pressure pulse.

4.3. Strain localisation and pore pressure build-up

330 The considerations above are restrained to the undrained system. The diffusion of pore
 331 fluids will tend to stabilise the pore pressure runaway (if it occurs) by draining the rock
 332 over a certain length scale. There is no general analytical solution available for equations
 333 of the form (11); here we restrict our analysis to a study of the stability of the system to
 334 small departures from equilibrium (which corresponds to $p_f = p_{\text{eq}}$).

335 As stated in Section 3.3, the experimental data of *Eggler and Ehmman* [2010] show that
 336 the near-equilibrium kinetics is linear, $n_r = 1$. In that case, the stability analysis detailed
 337 in Appendix C2 shows that pore pressure runaways are possible if $f' > f'_{\text{crit}}$ (same as

condition 30) and if the spatial wavelength of the perturbation λ is such that

$$\lambda > \lambda_{\text{crit}} = 2\pi \sqrt{\frac{p_{\text{eq}}(k/\eta)[1 - f'\beta/(h - h_{\text{crit}})]}{r_0 m_{\text{d}}^0 (1/\rho_{\text{f}} + \Delta_{\text{r}} V_{\text{s}})(1 - f'/f'_{\text{crit}})}}. \quad (31)$$

We observe that the critical wavelength depends on a number of parameters, some of them well constrained (equilibrium pressure p_{eq} , permeability k , fluid viscosity η , and the net volume change of the reaction), and others much more poorly known (essentially, all the parameters associated with the mechanical behaviour, including f' and β). However, as discussed above, the value of f' at the onset of the reaction is expected to be very large since small increments in porosity have large effects on the yield cap when the rock is initially non porous. We can use this fact to our advantage by noticing that the critical wavelength λ_{crit} tends to a constant, nonzero value for $f' \gg f'_{\text{crit}}$:

$$\lambda_{\text{crit}} \sim 2\pi \sqrt{\frac{p_{\text{eq}}(k/\eta)}{r_0 m_{\text{d}}^0 \Delta_{\text{r}} V_{\text{s}}} \sqrt{3} \frac{\nu - 1}{2\nu - 1} \frac{1}{\beta^{-1} - \beta_{\text{crit}}^{-1}}}. \quad (32)$$

Equation (32) provides a simple lower bound for the critical wavelength, which is, quite remarkably, independent from the hardening modulus h .

The value of λ_{crit} is shown in Figure 5 as a function of f' and β for the parameters relevant to the dehydration of antigorite into enstatite and forsterite. As expected, the wavelength tends to the constant given by (32) at large values of f' , and we confirm that this limit value has only a mild dependence (square root) on the dilatancy factor β .

Based on the parameter values outlined above for antigorite, we estimate typical values for λ_{crit} of the order of 10 to 100 m. In our model, this length scale corresponds to the characteristic width over which pore pressure builds up, and compaction (negative volumetric strain) localises.

4.4. Numerical tests

357 We performed a series of numerical computations in order to explore further the ef-
 358 fects of potential nonlinearities associated with the variations of mechanical, hydraulic
 359 and chemical parameters during deformation and reaction. We included a power-law
 360 dependence of the permeability on porosity, $k \propto \zeta^3$ (where we recall that ζ is the
 361 porosity of the rock minus its poroelastic variations), and accounted for depletion of
 362 antigorite by using a simple first-order approximation for the reactant surface area,
 363 $A_{\text{rlm}}/A_{\text{rlm}}^0 \approx (1 - \xi)$, in Equation (7). The numerical method is described fully in
 364 Appendix D, and the Matlab[®] implementation and source code is available online at
 365 http://github.com/nbrantut/Compaction_Dehydration. The solution for pore fluid
 366 pressure, strain, reaction progress and porosity is computed within a layer of width L ,
 367 with periodic boundary conditions, and an initial sinusoidal infinitesimal pore pressure
 368 perturbation is added to the homogeneous initial conditions. We chose a representative
 369 example by using an initial pore pressure of 3 GPa, an initial total mean stress of 3.61 GPa
 370 (i.e., an initial shear stress of 0.87 GPa), and an initial porosity of 3 %. Using the initial,
 371 reference parameters, we find that the critical wavelength for instability is $\lambda_{\text{crit}} \approx 0.08L$,
 372 so that we expect some compaction localisation (at least transiently).

373 The volumetric strain profile within the layer is shown as a function of time in Figure
 374 6(a). The initial ($\epsilon(y, 0) = 0$) and final (at $t \times r_0 = 100$) profiles are highlighted in black,
 375 and intermediate stages are shown light grey. Over time, a net volumetric strain local-
 376 isation develops around the centre of the layer, and remains there permanently at large
 377 times. The time evolution of the compaction localisation instability is better observed
 378 in Figure 6(b), which shows the volumetric strain in the centre of the layer ($y = 0$) and

379 on the edge ($y = \pm L/2$). The peak compaction at the centre develops quite rapidly,
380 initially accelerating, and then develops over a timescale of the order of $t \times r_0 \approx 10$, and
381 then stabilises. At the edges of the layer, the compaction develops more slowly and a
382 strong strain gradient develops in the initial phase of the instability; once the compaction
383 stabilises in the centre (at around $t \times r_0 \approx 20$), the strain becomes more homogeneous as
384 the edges also compact further until the whole process eventually stabilises, leaving only
385 a slight strain heterogeneity near the centre.

386 The evolution of all other key variables as a function of time is shown in Figure 7.
387 The onset of the compaction instability is marked by a rapid acceleration of the reaction
388 progress, porosity and pore pressure changes localised in the centre of the layer (solid
389 lines, $t \times r_0$ between 10 and 15). As the reaction progresses further the differences between
390 the reaction progress, porosity, strain and pore pressure at the centre and at the edges
391 progressively decrease. As the reaction approaches completion, the porosity stabilises at
392 around 27% while the pore pressure remains very high, corresponding to a mean effective
393 stress of around 0.07 GPa. At this point, no further compaction is possible because the
394 periodic boundary conditions effectively ensure that the system is undrained.

395 The full stress path of each material element in the layer is drawn in Figure 8 in the
396 effective mean stress, shear stress (p', τ) space. As the pore pressure and porosity increase
397 in the layer, the yield surface shrinks and the stress state evolves to maintain mechanical
398 equilibrium. The stress paths of different elements in the layer are not exactly the same,
399 since heterogeneities in pore pressure and stress develop between the centre (solid line)
400 and the edges (dashed line). As the reaction approaches completion, the effective stress
401 becomes very small ($p'/\sigma_n \approx 0.019$, i.e., $p' \approx 0.07$ GPa) and the material cannot compact

402 further because of the residual (small) nonzero strength, illustrated by the final yield
403 surface.

404 Overall, the numerical simulation confirms that a compaction instability is possible,
405 but that it is only transient as the system tends again to a homogeneous state while the
406 reaction approaches completion. The typical timescale for instability is of the same order
407 of magnitude as $1/r_0$, i.e., around 7 to 8 days. In our simulations, we impose periodic
408 boundary conditions so that the layer is effectively undrained: hence, the porosity and
409 pore pressure remain high after the reaction is completed. We performed complementary
410 simulations using drained boundaries as another end-member case scenario, and observed
411 that there is a long-term compaction occurring after the initial instability, and the pore
412 pressure returns progressively towards its equilibrium value over timescales determined
413 by the drained length across the layer.

5. Discussion

5.1. Model assumptions and limitations

414 The key assumption of the model presented here is that ductile deformation of antig-
415 orite is essentially time-independent. This approximation is justified by experimental
416 observations of antigorite deformation at elevated pressures and temperature, showing
417 that cataclastic mechanisms typically dominate [*Chernak and Hirth, 2010; Amiguet et al.,*
418 *2014; Auzende et al., 2015*] and that fully plastic flow is unlikely to occur due to the large
419 crystal anisotropy and lack of available slip systems in antigorite. Furthermore, partially
420 dehydrated serpentinite has also been shown to deform very similarly to porous sand-
421 stones [*Arkwright et al., 2008; Rutter et al., 2009*], which motivates the use of a closed
422 yield envelope.

423 However, there are also clear experimental indications that ductile flow of antigorite de-
424 pends on strain rate [e.g. *Hilaireret et al.*, 2007; *Amiguet et al.*, 2012], and time-dependency
425 may not be negligible if deformation occurs over very long timescales. We can test whether
426 time-dependent plastic flow contributes significantly to deformation by estimating the
427 strain rates developing during the instability in our model. As mentioned in the previous
428 Section, the characteristic timescale over which the instability develops is determined by
429 the reaction kinetics, $1/r_0$. The typical strain achieved during the instability is of the
430 order of a few percents, so that the strain rate is of the order of $r_0/100$, which is around
431 10^{-8} s^{-1} . Using that strain rate, the typical shear flow stress extrapolated from the plastic
432 flow laws given in *Amiguet et al.* [2012, their figure 6] is of the order of 0.1 GPa. Therefore,
433 our model based on time-independent ductile flow is broadly consistent with the rheology
434 of serpentinites as long as relatively low shear stresses are considered (around 0.1 GPa).

435 However, under near-isostatic conditions, the shear stress is not expected to be large
436 enough to produce significant viscous flow within the timescale of instability. The con-
437 tribution of viscous flow to isostatic compaction typically scales with the inverse of the
438 porosity [e.g. *Wilkinson and Ashby*, 1975; *McKenzie*, 1984], so that the driving effective
439 mean stress should be of the order of 1 GPa to achieve strain rates of around 10^{-8} s^{-1} for
440 a porosity of around 10%. It is therefore likely that viscous compaction in the absence of
441 shear stresses slows down the development of the pore pressure instability.

442 A number of coupled deformation-dehydration physical models have been developed
443 based on time-dependent rheology of rocks [e.g. *Connolly*, 1997; *Connolly and Podlad-*
444 *chikov*, 1998; *Connolly*, 2004; *Skarbek and Rempel*, 2016]. One key parameter exhibited
445 by these models is the compaction length scale, which is related to the hydraulic diffu-

446 sivity, compressibility and bulk viscosity of the rock. In this context, the timescale for
447 compaction is entirely determined by the rheology of the rock. In our approach using
448 time-independent ductile deformation, a characteristic length for pore pressure devel-
449 opment and compaction (λ_c , Equation (31)) also arises, associated with the hydraulic
450 diffusivity, rheology and reaction rate. This length λ_c is clearly analogue to the one ob-
451 tained from viscous compaction, and corresponds to the limiting case where the timescale
452 for compaction is determined by the reaction rate. For typical crustal metamorphic re-
453 actions, *Connolly* [1997] determines that the minimum compaction length is of the order
454 of 10 to 100 m. Quite interestingly, we find that the minimum compaction length in our
455 model is also of the order of 10 to 100 m for antigorite dehydration at intermediate depth
456 (see Figure 5). This similarity in compaction length scale between the two types of model
457 essentially arises from the similarity in timescales between viscous flow and reaction rate.

458 Here we made the assumption that the material deforms under isothermal conditions.
459 Although a full analysis including thermal effects is beyond the scope of the present
460 work, we discuss here qualitatively how changes in temperature can arise and modify the
461 behaviour of the material. Firstly, the dehydration reaction of antigorite is endothermic,
462 which constitutes a significant heat sink. Secondly, the irreversible work done by inelastic
463 deformation corresponds to energy dissipation and is a heat source. At 4 GPa and 625°C,
464 the enthalpy change of the reaction is 442 kJ per mole of antigorite (computed from the
465 database of *Holland and Powell* [1998]), i.e., around 2.5×10^2 MJ m⁻³. For a reaction
466 rate of the order of 10^{-8} s⁻¹, the rate of heat absorbed by the reaction is of the order of
467 2.5 J m⁻³ s⁻¹. The rate of work of the volumetric strain is given by $\dot{\epsilon}p'$, and for an effective
468 stress p' of around 100 MPa and a characteristic strain rate of the order of 10^{-8} s⁻¹, the

469 rate of heat generated by inelastic deformation is of the order of $1 \text{ J m}^{-3} \text{ s}^{-1}$. Although
470 the exact quantities are only approximate, the rate of heat absorbed by the reaction
471 and released by deformation are of the same order of magnitude, and might compensate
472 each other. If significant changes in temperature occur, for instance a cooling due to
473 the endothermic character of the reaction overcoming the heat generated by deformation,
474 the reaction kinetics will also be modified according to the corresponding change in ΔG
475 (Equation (5)). In that case, heat flow across the deformed/reacted zone might be the rate
476 limiting process. Assuming a heat diffusivity of $10^{-6} \text{ m}^2 \text{ s}^{-1}$, the characteristic diffusion
477 time across a layer of 100 m in thickness is 10^{10} s, and it drops to 10^8 s for a 10 m
478 width layer. Therefore, we expect heat flow to be limiting only when the deformation
479 (and reaction) rate becomes faster than 10^{-10} s^{-1} (respectively, 10^{-8} s^{-1}) in a thick
480 (respectively, thin) layer. In our simulations, such strain rates are achieved transiently
481 during the instability, so that thermal effects might affect the behaviour of the system
482 only after the instability has initiated.

483 Despite the limitations outlined above, the model formulation is quite general and could
484 be applicable to most devolatilisation reactions in subduction zones but also at shallower
485 depths in the crust. This is especially relevant for relatively cold parts of the crust (or
486 subduction zones), where the viscous creep rates of rocks are slow compared to reaction
487 kinetics, so that the hypothesis of time-independent rheology would be justified. Not all
488 reactions are expected to generate a pore pressure instability, and the surprising result here
489 is that instabilities only arise when the total volume change of the reaction is negative (i.e.,
490 at high pressure for antigorite). Under shallow crustal conditions, most devolatilisation
491 reactions are expected to produce a positive volume change, so instabilities should be

492 investigated on a case-by-case basis. In any case, the governing equation for pore pressure
493 (Equation (11)) remains valid and can be used to make predictions for fluid flow in active
494 prograde metamorphic settings, such as deep sedimentary basins (where gypsum and clay
495 mineral dehydrate), around rising plutons and magma chambers, and of course along
496 subduction zones.

5.2. Effective stress in subduction zones and implications for intermediate-depth earthquakes

497 One of the key outcome of our model is that antigorite dehydration at intermediate
498 depth results in a very rapid build-up of pore pressure, reducing the effective mean stress
499 towards near-zero values while maintaining a significant open porosity (at least as long as
500 the fluids are trapped inside the dehydrating layer). This pore pressure build-up occurs
501 despite the net negative volume change of the reaction, and is primarily driven by the
502 collapse of porosity. Hence, we expect the effective mean stress to remain near zero
503 throughout the regions where dehydration proceeds, independently from the net volume
504 change associated with the reaction. While this is also expected in models involving
505 viscous rock deformation, we find here that the path towards low effective stress states is
506 unstable, but only in the case when the net volume change is negative $1/\rho_f + \Delta_r V_s < 0$.
507 This instability arises because the compaction tends to increase pore pressure, and takes
508 the system further away from equilibrium. If the net volume change from the reaction is
509 positive, any compaction and pore collapse would increase pore pressure and bring the
510 system back to equilibrium, unless unrealistic amounts of shear-induced dilatancy occur.

511 One interesting outcome of our model is that we show that the dehydration and com-
512 paction process produces significant shear deformation in the rock, and not just pure

513 volumetric compaction. In our approach, we used uniaxial strain boundary conditions in
514 order to simulate a simple, tractable problem. In nature, the stress state and boundary
515 conditions are necessarily more complex. The existence of shear stresses, even very small
516 (0.01 to 0.1 GPa), is expected to produce significant shear strains during the pore pres-
517 sure build-up. The dehydrating body of antigorite then acts as a very deformable layer
518 or inclusion, amplifying the stresses around it. In addition, pore fluid diffusion outside
519 the dehydrating body also contributes to decreasing the effective stress in the surrounding
520 rocks.

521 The combination of relatively rapid stress amplification and effective pressure reduction
522 provides a reasonable mechanism for the inception of brittle deformation in the surround-
523 ing ultramafic rocks (peridotites and metagabbros). Indeed, at the temperatures and
524 pressures relevant to antigorite dehydration and at strain rates as high as 10^{-8} s^{-1} during
525 the pore pressure instability, peridotites have a high strength and are unlikely to acco-
526 modate deformation in a purely viscous manner, thus raising elastic stresses and favoring
527 brittle deformation. Such a mechanism is essentially a kind of dehydration embrittle-
528 ment, but in the surrounding rocks and not in the dehydrating serpentinite itself. While
529 this process had been suggested in earlier works by Kirby [1987] or Rutter *et al.* [2009],
530 our model provides first-order quantitative constraints on its likelihood by establishing
531 a closed-form stability criterion that depends on the rock rheology and reaction kinetics
532 (Equation (28)).

533 As a final note of caution regarding our interpretations in terms of fluid pressure at
534 intermediate depths, we recall here that the concept of effective stress makes sense only
535 if a uniform pore pressure can be defined for a representative volume element of the rock.

536 This is most likely the case when porosity is larger than several percents, above the per-
537 colation threshold [Guéguen and Palciauskas, 1994]. However, over long timescales, the
538 progressive drainage of the pore fluid outside of the dehydrating zones tends to allow com-
539 paction to reduce porosity; this reduction in porosity occurs concomitantly with surface
540 diffusion and dissolution-precipitation processes that heal and seal the pore space, leaving
541 a disconnected pore network and free fluids present only as fluid inclusions [e.g. Smith and
542 Evans, 1984]. In the long term, pore pressure is not a well defined concept and neither
543 is effective stress. There are currently insufficient constrains on healing mechanisms in
544 silicates to draw definitive quantitative conclusions on the persistence and connectivity of
545 the pore space at intermediate depths in subduction zones, but we expect that the short
546 timescale of the instability (typically of the order of 10 days in our simulations) and the
547 large porosity generated by the reaction (around 20%) ensure a reasonable pore network
548 connectivity and validates the use of the concept of effective stress.

6. Conclusions

549 We developed a model to simulate coupled deformation and dehydration of antigorite at
550 intermediate depths in subduction zones. Our model shows that dehydration can lead to
551 unstable pore pressure rise and deformation when the net volume change of the reaction
552 is negative, due to a positive feedback between pore fluid pressure, compaction and de-
553 hydration rate. The stability criterion (Equation (30)) is controlled by the dependence of
554 the yield envelope on porosity (parameter $f' = \partial f / \partial \zeta$); using estimates for f' consistent
555 with well established mechanics of porous rocks, we find that antigorite dehydration leads
556 to unstable deformation under typical intermediate-depth conditions in subduction zones.

557 Furthermore, we also show that the instability is associated with localised deformation
 558 and fluid pressure over a characteristic length scale controlled by hydraulic diffusivity,
 559 rheological parameters and reaction rate. A lower bound for this characteristic length
 560 is of the order of 10 to 100 m, commensurate with the viscous compaction length scale
 561 obtained in models using time-dependent rheologies.

562 Our model predicts that the typical strain rates during the instability are of the order
 563 of 10^{-8} s^{-1} . At such rates and at the relatively cool dehydration temperature of antig-
 564 orite (around 600°C), the surrounding, chemically stable peridotites and metagabbroic
 565 rocks forming the subducted slab have a high strength, and are expected to build up
 566 elastic stresses. The elevated pore pressures associated with the dehydration reaction can
 567 therefore transiently bring the surrounding rocks back into the brittle field, thus allowing
 568 the nucleation and propagation of earthquakes. This mechanism is clearly a type of de-
 569 hydration embrittlement, but is crucially based on a rapid stress transfer between weak
 570 dehydrating rocks and strong surrounding ultramafic rocks, in a manner conceptually
 571 similar to the early model of Kirby [1987] for transformation-induced instabilities.

Appendix A: Derivation of governing equations

A1. Fluid pressure

572 For a reacting porous medium, the continuity equations for the solid skeleton and the
 573 fluid are [Coussy, 2004]

$$\frac{\partial(\rho_s(1-n))}{\partial t} + \text{div}(\rho_s(1-n)\mathbf{v}_s) = -r, \quad (\text{A1})$$

$$\frac{\partial(n\rho_f)}{\partial t} + \text{div}(n\rho_f\mathbf{v}_f) = +r, \quad (\text{A2})$$

574 where ρ_s is the density of the solid, ρ_f is the density of the fluid, n is the Eulerian porosity,
 575 \mathbf{v}_s is the velocity of the solid and \mathbf{v}_f is the velocity of the fluid. In the above equations,
 576 r denotes the rate at which fluid mass is generated from solid mass. This will be our
 577 definition for the reaction rate. Neglecting gradients in ρ_s and ρ_f , the combination of
 578 equations A1 and A2 leads to

$$\frac{1-n}{\rho_s} \frac{\partial \rho_s}{\partial t} + \frac{n}{\rho_f} \frac{\partial \rho_f}{\partial t} + \operatorname{div}(\mathbf{v}_s) + \operatorname{div}(n(\mathbf{v}_f - \mathbf{v}_s)) = r(1/\rho_s - 1/\rho_f). \quad (\text{A3})$$

579 We can relate the divergence of the relative fluid velocity with respect to the solid to
 580 the gradient in fluid pressure by using Darcy's law [*Coussy*, 2004]:

$$n(\mathbf{v}_f - \mathbf{v}_s) = -(k/\eta)\operatorname{grad}(p_f), \quad (\text{A4})$$

581 where p_f is the fluid pressure, k is the permeability of the material, and η is the viscosity
 582 of the fluid. The divergence of the velocity of the solid is the bulk volumetric (Eulerian)
 583 strain rate:

$$\operatorname{div}(\mathbf{v}_s) = \frac{\partial \epsilon}{\partial t}, \quad (\text{A5})$$

584 where ϵ is the bulk volumetric strain. The combination of relations A4 and A5 with
 585 equation A3 yields:

$$\frac{1-n}{\rho_s} \frac{\partial \rho_s}{\partial t} + \frac{n}{\rho_f} \frac{\partial \rho_f}{\partial t} + \frac{\partial \epsilon}{\partial t} - \frac{k}{\eta} \nabla^2 p_f = r(1/\rho_s - 1/\rho_f). \quad (\text{A6})$$

586 The variation of the fluid density can be expressed as

$$\frac{1}{\rho_f} \frac{\partial \rho_f}{\partial t} = c_f \frac{\partial p_f}{\partial t}, \quad (\text{A7})$$

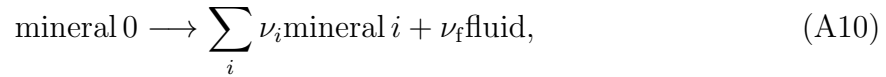
587 where c_f is the compressibility of the fluid. The variation of the solid density is decomposed
 588 into two contributions:

$$\frac{1}{\rho_s} \frac{\partial \rho_s}{\partial t} = c_s \frac{\partial p_s}{\partial t} + \frac{1}{\rho_s} \frac{\partial \rho_s}{\partial m} r, \quad (\text{A8})$$

589 where c_s is the compressibility of the constituents of the solid skeleton, and m denotes the
 590 mass of fluid released by the chemical reaction. The last term in A8 corresponds to the
 591 evolution of the average density of the solid skeleton as the reaction proceeds (this term
 592 would be zero if the solid was transforming entirely into a fluid, without generating solid
 593 products). Combining relations A7 and A8 into equation A6 yields:

$$((1-n)c_s + nc_f) \frac{\partial p_f}{\partial t} = \frac{k}{\eta} \nabla^2 p_f - \frac{\partial \epsilon}{\partial t} + r \left(\frac{1}{\rho_f} - \frac{1}{\rho_s} - \frac{1-n}{\rho_s} \frac{\partial \rho_s}{\partial m} \right). \quad (\text{A9})$$

594 We now need to express the evolution of the average density of the solid as a function
 595 of the reaction progress. We are interested in the following type of chemical reaction:



596 where $\nu_{i,f}$ are stoichiometric coefficients. Denoting ξ the reaction progress and m_d^0 the
 597 total mass of fluid that can be released by the reaction (per unit volume of rock), the
 598 solid volume is expressed as

$$V_s = \frac{m_d^0}{\nu_f M_f} \left(M_0(1-\xi)/\rho_0 + \sum_i (\nu_i M_i / \rho_i) \xi \right), \quad (\text{A11})$$

599 where M_i is the molar mass of constituent i . The average solid mass is denoted m_s . The
 600 density of the solid is $\rho_s = m_s/V_s$; hence we have:

$$\frac{1}{\rho_s} \frac{\partial \rho_s}{\partial m} = \frac{1}{m_s} \frac{\partial m_s}{\partial m} - \frac{1}{V_s} \frac{\partial V_s}{\partial m}. \quad (\text{A12})$$

601 The conservation of mass imposes that $\partial m_s / \partial m = -1$, so that

$$\frac{1}{\rho_s} \frac{\partial \rho_s}{\partial m} = \frac{1}{V_s} \left(-\frac{1}{\rho_s} - \frac{\partial V_s}{\partial m} \right). \quad (\text{A13})$$

602 The last term in parenthesis of the previous equation corresponds to the solid volume
 603 change of the reaction, which we denote $\Delta_r V_s$. Keeping in mind that $m = m_d^0 \xi$, we can

604 use relation A11 to express $\Delta_r V_s$ as

$$\Delta_r V_s = -\frac{M_0}{\rho_0 \nu_f M_f} + \frac{\sum_i \nu_i M_i / \rho_i}{\nu_f M_f}. \quad (\text{A14})$$

605 Finally, we have to keep in mind that $V_s = 1 - n$ by definition, so that equation A13

606 becomes

$$\frac{1 - n}{\rho_s} = -\frac{1}{\rho_s} - \Delta_r V_s. \quad (\text{A15})$$

607 The combination of the relation above with the mass balance equation A9, eventually

608 leads to the governing equation (1) for pore fluid pressure.

A2. Constitutive behaviour

609 We assume that the dehydrating rock is elasto-plastic. We introduce the yield function
 610 $f(\sigma, \zeta)$, where σ is the stress tensor and ζ is an internal variable on which the yield
 611 cap depends. ζ can be identified to either the finite porosity of the material, or more
 612 directly to the reaction progress in the case of a pure chemical control over the material's
 613 strength. These two options will be discussed later on. We also assume, in accordance
 614 with experimental observations, that the material undergoes strain hardening. For the
 615 sake of simplicity, f and g were assumed linear in terms of τ . In that case, the consistency
 616 condition for plastic loading is therefore

$$\left(\frac{\partial f}{\partial \sigma}\right)^T d\sigma + \frac{\partial f}{\partial \zeta} d\zeta - h d\lambda = 0, \quad (\text{A16})$$

617 where h is the hardening modulus and $d\lambda$ is a positive infinitesimal scalar (so-called
 618 plastic increment). If we now introduce the plastic potential $g(\sigma)$, the elasto-plastic stress
 619 increment is then given by

$$d\sigma = \mathbf{M}^{\text{el}} d\epsilon - d\lambda \mathbf{M}^{\text{el}} \frac{\partial g}{\partial \sigma}, \quad (\text{A17})$$

620 where \mathbf{M}^{el} is the elastic tensor and ϵ is the total strain tensor. The combination of
 621 equations A16 and A17 allows the determination of the plastic increment $d\lambda$ and yields
 622 the full incremental constitutive relation

$$d\sigma = \mathbf{M}^{\text{ep}}d\epsilon + \Psi d\zeta, \quad (\text{A18})$$

623 where

$$\mathbf{M}^{\text{ep}} = \mathbf{M}^{\text{el}} - \frac{\mathbf{M}^{\text{el}} \frac{\partial g}{\partial \sigma} \left(\frac{\partial f}{\partial \sigma} \right)^{\text{T}} \mathbf{M}^{\text{el}}}{h + \left(\frac{\partial f}{\partial \sigma} \right)^{\text{T}} \mathbf{M}^{\text{el}} \frac{\partial g}{\partial \sigma}} \quad (\text{A19})$$

624 and

$$\Psi = - \frac{\mathbf{M}^{\text{el}} \frac{\partial f}{\partial \zeta} \frac{\partial g}{\partial \sigma}}{h + \left(\frac{\partial f}{\partial \sigma} \right)^{\text{T}} \mathbf{M}^{\text{el}} \frac{\partial g}{\partial \sigma}}. \quad (\text{A20})$$

625 We further assume that the material is isotropic. The scalars p' and τ are used here
 626 and they represent, respectively, the Terzaghi effective mean stress (i.e. the difference
 627 between the total mean stress and the pore pressure, $p' = \text{tr}(\sigma)/3 + p_f$) and the shearing
 628 stress intensity. The shearing stress intensity τ is defined as the square root of the second
 629 invariant of the deviatoric part, s , of the stress tensor: $\tau = \sqrt{\frac{1}{2}s_{ij}s_{ij}}$. The Einstein
 630 summation convention is adopted and the indices i, j take values 1, 2, 3. In the (p', τ)
 631 space, the stress vector σ is defined as:

$$\sigma = \begin{pmatrix} p' \\ \tau \end{pmatrix}. \quad (\text{A21})$$

632 Likewise, the strain vector can be described by the volumetric strain ϵ and shear strain γ :

$$\epsilon = \begin{pmatrix} \epsilon \\ \gamma \end{pmatrix}. \quad (\text{A22})$$

633 The elastic tensor is written then:

$$\mathbf{M}^{\text{el}} = \begin{pmatrix} K & 0 \\ 0 & G \end{pmatrix}, \quad (\text{A23})$$

634 where K is the bulk modulus of the porous material, and G its shear modulus. For a
 635 general plastic behaviour, the derivatives of the yield function and plastic potential are
 636 expressed as follows:

$$\frac{\partial f}{\partial \sigma} = \begin{pmatrix} \mu \\ 1 \end{pmatrix}, \quad \frac{\partial g}{\partial \sigma} = \begin{pmatrix} \beta \\ 1 \end{pmatrix}, \quad (\text{A24})$$

637 where μ is the friction coefficient, and β the dilatancy factor. For the sake of simplicity,
 638 f and g were assumed linear in terms of τ . The full expression for the incremental stress-
 639 strain relation in the (p', τ) space becomes:

$$dp' = \frac{GK [(1 + h/G)d\epsilon - \beta d\gamma]}{h + G + \beta\mu K} - \frac{\beta K}{h + G + \beta\mu K} \frac{\partial f}{\partial \zeta} d\zeta, \quad (\text{A25})$$

$$d\tau = \frac{GK [-\mu d\epsilon + (h/K + \beta\mu)d\gamma]}{h + G + \beta\mu K} - \frac{G}{h + G + \beta\mu K} \frac{\partial f}{\partial \zeta} d\zeta. \quad (\text{A26})$$

640 In expressions A25 and A26, the factor $\partial f/\partial \zeta$ corresponds to the dependency of the
 641 yield cap on the internal variable (or material parameter) ζ . As summarised by *Wong*
 642 *and Baud* [2012], yield caps for porous rocks can be scaled by the critical pressure for
 643 hydrostatic pore collapse, usually denoted P^* . It has also been observed [e.g. *Zhang*
 644 *et al.*, 1990] that P^* is scaled by the product of the grain size and the porosity of the rock,
 645 to the power 3/2. This dependency of f on P^* , and of P^* on porosity implies that the yield
 646 cap can be considered as a function of the porosity of the rock. Hence, a natural choice
 647 for the parameter ζ is the total nominal porosity (i.e., the current finite porosity resulting
 648 from deformation and reaction, minus any variations produced by elastic deformations).
 649 In such a framework, we can write

$$d\zeta = -m_d^0 \Delta_r V_s d\xi + d\epsilon - dp'/K. \quad (\text{A27})$$

650 Using this expression for ζ into Equations (A25) and (A26), we finally arrive at the
 651 incremental constitutive formulation of Equations (3) and (4) in the main text.

A3. Uniaxial compaction

652 The combination of relations 10 and 3 yields

$$\frac{\partial p}{\partial t} + \frac{\partial p_f}{\partial t} = \frac{GK \left[(1 + (h - f'\beta)/G) + 2\beta/\sqrt{3} \right] \frac{\partial \epsilon}{\partial t} - \frac{f'\beta K}{h - f'\beta + G + \beta\mu K} \frac{\partial \xi}{\partial t}}{h - f'\beta + G + \beta\mu K}. \quad (\text{A28})$$

653 Assuming a constant σ_n over time, equation 9 yields

$$\frac{\partial p}{\partial t} = \frac{2}{\sqrt{3}} \frac{\partial \tau}{\partial t}, \quad (\text{A29})$$

654 which we combine to equation A28, making use of relation 4, to obtain

$$\frac{\partial p_f}{\partial t} = M \frac{\partial \epsilon}{\partial t} - f'X \frac{\partial \xi}{\partial t}, \quad (\text{A30})$$

655 where

$$M = \frac{GK}{h - f'\beta + G + \beta\mu K} \left[\left(1 + \frac{2}{\sqrt{3}}\mu \right) \left(1 + \frac{2}{\sqrt{3}}\beta \right) + (h - f'\beta) \left(\frac{1}{G} + \frac{4}{3K} \right) \right], \quad (\text{A31})$$

656 and

$$X = -m_d^0 \Delta_r V_s \frac{\beta K - 2G/\sqrt{3}}{h - f'\beta + G + \beta\mu K}. \quad (\text{A32})$$

657 Now we can use equation 1 to express the volumetric strain rate:

$$\frac{\partial \epsilon}{\partial t} = \frac{k}{\eta} \frac{\partial^2 p_f}{\partial y^2} + (m_d^0 (1/\rho_f + \Delta_r V_s)) \frac{\partial \xi}{\partial t} - c_b \frac{\partial p_f}{\partial t}. \quad (\text{A33})$$

658 We finally use the expression of the volumetric strain rate given by A33 into equation A30

659 to obtain

$$\frac{\partial p_f}{\partial t} = \frac{Mk/\eta}{1 + c_b M} \frac{\partial^2 p_f}{\partial y^2} + \frac{Mm_d^0 (1/\rho_f + \Delta_r V_s) - f'X}{1 + c_b M} \frac{\partial \xi}{\partial t}. \quad (\text{A34})$$

660 Using the chemical kinetics established in Equation 7, we finally arrive at Equation (11)

661 of the main text.

Appendix B: Volume change for antigorite dehydration

662 The density of a phase as a function of temperature is given by

$$\rho(T) = \rho^\circ e^{-\Phi}, \quad (\text{B1})$$

663 where ρ° is the density under standard conditions (at $T = T_0 = 25^\circ\text{C}$), and

$$\Phi = \ln(V_m(T)/V_m^\circ) = \alpha^\circ \left(T - T_0 - 20(\sqrt{T} - \sqrt{T_0}) \right). \quad (\text{B2})$$

664 The density as a function of pressure is given by

$$\rho(P) = \rho^\circ (1 + 2\ell)^{3/2}, \quad (\text{B3})$$

665 where ℓ is the linear strain calculated from the bulk modulus K and its derivative with

666 pressure $K' = \partial K / \partial P$:

$$P/K = 3\ell(1 + 2\ell)^{5/2} \left[1 - 2(3 - 3K'/4)\ell + \frac{\ell^2}{6} (4(3 - 3K'/4)(4 - 3K') + 5(3K' - 5)) \right]. \quad (\text{B4})$$

667 The total change in density as a function of pressure and temperature is finally obtained

668 from

$$\rho(P, T) = [\rho(P)/\rho^\circ] \rho(T), \quad (\text{B5})$$

669 which implies that the molar volume is

$$V_m(P, T) = M/\rho(P, T) = V_m^\circ (1 + 2\ell)^{-3/2} e^\Phi. \quad (\text{B6})$$

Appendix C: Stability analysis

C1. Derivation of criterion

670 The inequality (28) can be rewritten as

$$f' \left[\Delta_r V_s (\beta K - 2G/\sqrt{3}) - \beta (K + 4G/3) (1/\rho_f + \Delta_r V_s) \right] > -(K + 4G/3) (h - h_{\text{crit}}) (1/\rho_f + \Delta_r V_s). \quad (\text{C1})$$

671 Assuming that the material is nominally stable, i.e, $h > h_{\text{crit}}$, and considering that the
 672 reaction has a total negative volume change ($1/\rho_f + \Delta_r V_s < 0$), the rhs of Inequality (C1)
 673 is a positive quantity. If the term in brackets on the lhs is negative, f' would have to be
 674 also negative in order to satisfy the inequality. This is a contradiction since the material
 675 is porosity-softening and $f' > 0$. So a first requirement for the instability to be possible
 676 is that the bracketed term is positive, which implies that

$$\beta \left[\frac{1}{\rho_f} + \frac{4G}{3K + 4G} \Delta_r V_s \right] < \frac{2}{\sqrt{3}} \frac{-3G}{3K + 4G} \Delta_r V_s. \quad (\text{C2})$$

677 Considering that the material is compactant ($\beta < 0$) and that the solid volume change of
 678 the reaction is negative ($\Delta_r V_s < 0$), Inequality (C2) is satisfied when either

$$\frac{1}{\rho_f} + \frac{4G}{3K + 4G} \Delta_r V_s > 0, \quad (\text{C3})$$

679 OR

$$\frac{1}{\rho_f} + \frac{4G}{3K + 4G} \Delta_r V_s < 0 \text{ and } \beta > \beta_{\text{crit}}, \quad (\text{C4})$$

680 where β_{crit} is defined in Equation (29) of the main text. In that case, the instability
 681 criterion in terms of f' is given by (see Equation (C1))

$$f' > \frac{-(K + 4G/3)(h - h_{\text{crit}})(1/\rho_f + \Delta_r V_s)}{\Delta_r V_s(\beta K - 2G/\sqrt{3}) - \beta(K + 4G/3)(1/\rho_f + \Delta_r V_s)}, \quad (\text{C5})$$

682 which is exactly the same as Equation (30) after some rearrangements.

C2. Linear analysis

683 Denoting p'_f the small perturbation of p_f above p_{eq} , we rewrite the governing equation
 684 for pore pressure (11) as follows:

$$\frac{\partial p'_f}{\partial t} = \frac{Mk/\eta}{1 + c_b M} \frac{\partial^2 p'_f}{\partial y^2} + \frac{Mm_d^0(1/\rho_f + \Delta_r V_s) - f'X}{1 + c_b M} r_0 \left(\frac{p'_f}{p_{\text{eq}}} \right)^{n_r}. \quad (\text{C6})$$

685 The qualitative behaviour of the system depends on the value of n_r .

686 For $n_r = 1$ (i.e., the dehydration reaction kinetics is approximated to be first-order),
 687 the equation is linear and we can perform a linear stability analysis to explore how the
 688 system evolves. We assume no flux conditions at the boundaries of a dehydrating layer
 689 of thickness W (which simulates a serpentinite layer embedded in an impermeable host
 690 rock). Then we look for solutions of (C6) (with $n_r = 1$) in the form

$$p'_f = A \cos(2\pi y/\lambda) \exp(St), \quad (\text{C7})$$

691 where A is the amplitude of the perturbation, S is its growth factor, and λ is its wave-
 692 length. Our suggested solution must be consistent with the prescribed boundary con-
 693 ditions, hence we require that $\lambda = W/k$, ($k = 1, 2, \dots$). The perturbation is unstable
 694 ($S > 0$) if (1) $f' > f'_{\text{crit}}$ and (2) the wavelength is greater than a critical wavelength λ_{crit} :

$$\lambda > \lambda_{\text{crit}} = 2\pi \sqrt{\frac{p_{\text{eq}} k / \eta}{r_0 [m_d^0 (1/\rho_f + \Delta_r V_s) - f' X / M]}}. \quad (\text{C8})$$

695 After some algebra, the critical wavelength can be rewritten as in (31) in the main text.

696 For $n_r > 1$, the situation is mathematically more complicated. Indeed, one can imme-
 697 diately observe in equation (C6) that the reaction term does *not* appear in a first order
 698 stability analysis (it is elevated to a power greater than 1). However, one could hope to
 699 make useful analytical predictions without resorting to a full numerical treatment. Let us
 700 assume that the perturbation has a characteristic amplitude A and a characteristic length
 701 scale L , i.e., $p'_f(y, t) = A(t)g(y/L(t))$ where g is a non dimensional function of the order
 702 of 1. The governing equation for p'_f is then

$$\frac{\partial p'_f}{\partial t} = \frac{A}{L^2} \frac{Mk/\eta}{1 + c_b M} g''(y/L) + \frac{Mm_d^0(1/\rho_f + \Delta_r V_s) - f'X}{1 + c_b M} r_0 A^{n_r} g^{n_r}(y/L). \quad (\text{C9})$$

703 The reaction term will be dominant, i.e., the system will be *unstable*, if

$$L \gg \sqrt{\frac{1}{A^{n_r-1}} \frac{p_{\text{eq}} k / \eta}{r_0 [m_d^0 (1/\rho_f + \Delta_r V_s) - f' X/M]}} = \frac{A^{(1-n_r)/2}}{2\pi} \lambda_{\text{crit}}. \quad (\text{C10})$$

704 The condition given in (C10) is very similar to the one obtained in (C8) for the linear
 705 case, but here we see that the amplitude of the perturbation A appears in the definition
 706 of the critical length scale. Hence, according to (C10), the system is unstable only if the
 707 wavelength *and the amplitude* of the perturbations are large enough to overcome diffusion.
 708 In any case, we note that the reaction will only dominate the system at early times; one can
 709 show that diffusion cannot be neglected everywhere when the system evolves with time.
 710 Here we are only interested in the behaviour at early times, because we have assumed
 711 that the parameters of the equations are constant. For further evolution of the system,
 712 the full nonlinearities should be included and it is not worth going too far mathematically
 713 with our simplified system.

Appendix D: Numerical methods

The numerical solution of the fully coupled, nonlinear system is obtained by discretising the governing equation for pore pressure (11) in space using a centered finite difference stencil, and then solving for reaction progress, pore pressure, volumetric strain, total mean stress, porosity and shear stress as a coupled system of ordinary differential equations (ODEs). In practice, we normalise the governing equations by using the magnitude of the imposed total normal stress σ_n as the stress scale, the reaction rate $1/r_0$ as the time scale, and the thickness of the antigorite layer (denoted L). We use a centered finite difference approximation of the second-order spatial derivatives of pore pressure, with a grid defined by points $y_i = i\Delta y$, and implement periodic boundary conditions at the edges $y = 0$ and

$y/L = 1$. The full system of ODEs is then:

$$\frac{\partial \xi_i}{\partial t} = s(1 - \xi_i) |p_{fi}/p_{eq} - 1|^{n_r}, \quad (D1)$$

$$\begin{aligned} \frac{\partial p_{fi}}{\partial t} = \frac{M}{1 + c_b M} \frac{1}{\eta \Delta y^2} & (k_{i+1/2}(p_{fi+1} - p_{fi}) - k_{i-1/2}(p_{fi} - p_{fi-1})) \\ & + \frac{M m_d^0 (1/\rho_f + \Delta_r V_s) - f' X}{1 + c_b M} \frac{\partial \xi_i}{\partial t}, \end{aligned} \quad (D2)$$

$$\frac{\partial \epsilon_i}{\partial t} = \frac{1}{M} \left(\frac{\partial p_{fi}}{\partial t} + f' X \frac{\partial \xi_i}{\partial t} \right), \quad (D3)$$

$$\frac{\partial p_i}{\partial t} = \frac{1}{\sqrt{3}/2 + \beta - f'/K} \left((f'/K - \beta) \frac{\partial p_{fi}}{\partial t} - f' \frac{\partial \epsilon_i}{\partial t} + f' m_d^0 \Delta_r V_s \frac{\partial \xi_i}{\partial t} \right), \quad (D4)$$

$$\frac{\partial \zeta_i}{\partial t} = -m_d^0 \Delta_r V_s \frac{\partial \xi_i}{\partial t} + \frac{\partial \epsilon_i}{\partial t} - \frac{1}{K} \left(\frac{\partial p_i}{\partial t} + \frac{\partial p_{fi}}{\partial t} \right), \quad (D5)$$

$$\frac{\partial \tau_i}{\partial t} = -\beta \left(\frac{\partial p_i}{\partial t} + \frac{\partial p_{fi}}{\partial t} \right) - f' \frac{\partial \xi_i}{\partial t}, \quad (D6)$$

where subscripts i indicate variables at point x_i , and

$$k_{i\pm 1/2} = (k_i + k_{i\pm 1})/2. \quad (D7)$$

In addition, a consistency check is performed by computing the total normal stress:

$$\frac{\partial \sigma_{ni}}{\partial t} = \frac{\partial p_i}{\partial t} - \frac{2}{\sqrt{3}} \frac{\partial \tau_i}{\partial t}, \quad (D8)$$

714 and verifying a posteriori that it remains constant throughout space and time. All
 715 the parameters that are stress dependent, namely, β , μ and f' , are updated at every
 716 time and space step to account for the nonlinearities. The ODEs are solved by using
 717 Matlab's `ode15s` solver. The full Matlab code is available online at the following url:
 718 www.github.com/nbrantut/Compaction_Dehydration.git.

719 **Acknowledgments.** This work was supported by the UK Natural Environment Re-
 720 search Council through grants NE/K009656/1 and NE/M016471/1 to NB. We are thank-
 721 ful to Bruce Hobbs and John Rudnicki for their valuable review comments.

References

- 722 Amiguet, E., B. Reynard, R. Caracas, B. Van de Moortèle, N. Hilaret, and Y. Wang,
723 Creep of phyllosilicates at the onset of plate tectonics, *Earth Planet. Sci. Lett.*, 345-348,
724 142–150, 2012.
- 725 Amiguet, E., B. Van de Moortèle, P. Cordier, N. Hilaret, and B. Reynard, Deformation
726 mechanisms and rheology of serpentines in experiments and in nature, *J. Geophys. Res.*,
727 119, doi:10.1002/2013JB010791, 2014.
- 728 Arkwright, J. C., E. H. Rutter, K. H. Brodie, and S. Llana-Fúnez, Role of porosity
729 and dehydration reactions on the deformation of hot-pressed serpentinite aggregates, *J.*
730 *Geol. Soc. London*, 165, 639–649, 2008.
- 731 Auzende, A.-L., J. Escartin, N. P. Walte, S. Guillot, G. Hirth, and D. J. Frost, Deformation
732 mechanics of antigorite serpentinite at subduction zone conditions from experimentally
733 and naturally deformed rocks, *Earth Planet. Sci. Lett.*, 411, 229–240, 2015.
- 734 Bezacier, L., B. Reynard, J. D. Bass, C. Sanchez-Valle, and B. Van de Moortèle, Elasticity
735 of antigorite, seismic detection of serpentinites, and anisotropy in subduction zones,
736 *Earth Planet. Sci. Lett.*, 289, 198–208, 2010.
- 737 Brantut, N., and J. Sulem, Strain localisation and slip instability in a strain-rate
738 hardening, chemically weakening material, *J. Appl. Mech.*, 73(3), 031004, doi:
739 10.1115/1.4005880, 2012.
- 740 Chernak, L. J., and G. Hirth, Deformation of antigorite serpentinite at high temperature
741 and pressure, *Earth Planet. Sci. Lett.*, 29, 23–33, 2010.
- 742 Connolly, J. A. D., Devolatilization-generated fluid pressure and deformation-propagated
743 fluid flow during prograde regional metamorphism, *J. Geophys. Res.*, 102(B8), 18,149–

- 744 18,173, 1997.
- 745 Connolly, J. A. D., The mechanics of metamorphic fluid expulsion, *Elements*, 6, 165–172,
746 2004.
- 747 Connolly, J. A. D., and Y. Y. Podladchikov, Compaction-driven fluid flow in viscoelastic
748 rock, *Geodin. Acta*, 11(2-3), 55–84, 1998.
- 749 Connolly, J. A. D., and Y. Y. Podladchikov, Fluid flow in compressive tectonic settings:
750 Implications for midcrustal seismic reflectors and downward fluid migration, *J. Geophys.*
751 *Res.*, 109, B04201, doi:10.1029/2003JB002822, 2004.
- 752 Coussy, O., *Poromechanics*, John Wiley & Sons, Ltd, Chichester, England, 2004.
- 753 Eggler, D. H., and A. N. Ehmann, Rate of antigorite dehydration at 2 GPa applied to
754 subduction zones, *Am. Min.*, 95, 761–769, 2010.
- 755 Escartín, J., G. Hirth, and B. Evans, Nondilatant brittle deformation of serpentinites:
756 Implications for Mohr-Coulomb theory and the strength of faults, *J. Geophys. Res.*,
757 102(B2), 2897–2913, 1997.
- 758 Guéguen, Y., and V. Palciauskas, *Introduction to the Physics of Rocks*, Princeton Univer-
759 sity Press, Princeton, New Jersey (USA), 1994.
- 760 Hacker, B. R., G. A. Abers, and S. M. Peacock, Subduction factory 1. Theoretical min-
761 eralogy, densities, seismic wave speeds, and H₂O content, *J. Geophys. Res.*, 108(B1),
762 2029, doi:10.1029/2001JB001127, 2003a.
- 763 Hacker, B. R., S. M. Peacock, G. A. Abers, and S. D. Holloway, Subduction factory 2. Are
764 intermediate-depth earthquakes in subducting slabs linked to metamorphic dehydration
765 reactions?, *J. Geophys. Res.*, 108(B1), 2030, doi:10.1029/2001JB001129, 2003b.

- 766 Hilaret, N., B. Reynard, Y. Wang, I. Daniel, S. Merkel, N. Nishiyama, and S. Petit-
767 girard, High-pressure creep of serpentine, interseismic deformation, and initiation of
768 subduction, *Science*, *318*(5858), 1910–1913, 2007.
- 769 Holland, T. J. B., and R. Powell, An internally consistent thermodynamic data set for
770 phases of petrological interest, *J. Metamorphic Geol.*, *16*, 309–343, 1998.
- 771 Issen, K. A., and J. W. Rudnicki, Conditions for compaction bands in porous rock, *J.*
772 *Geophys. Res.*, *105*(B9), 21,529–21,536, 2000.
- 773 Jung, H. H., H. W. Green, and L. F. Dobrzhinetskaya, Intermediate depth earthquake
774 faulting by dehydration embrittlement with negative volume change, *Nature*, *428*, 545–
775 549, 2004.
- 776 Kirby, S. H., Localized polymorphic phase transformations in high-pressure faults and
777 applications to the physical mechanism of deep earthquakes, *J. Geophys. Res.*, *92*(B13),
778 13,789–13,800, 1987.
- 779 Lasaga, A. C., and D. M. Rye, Fluid flow and chemical reaction kinetics in metamorphic
780 systems, *Am. J. Sci.*, *293*, 361–404, 1993.
- 781 McKenzie, D., The generation and compaction of partially molten rock, *J. Petrol.*, *25*(3),
782 713–765, 1984.
- 783 Murrell, S. A. F., and I. A. H. Ismail, The effect of decomposition of hydrous minerals on
784 the mechanical properties of rocks, *Tectonophysics*, *31*, 207–258, 1976.
- 785 Proctor, B., and G. Hirth, “Ductile to brittle” transition in thermally stable antigorite
786 gouge at mantle pressures, *J. Geophys. Res.*, *121*, doi:10.002/2015JB012710, 2016.
- 787 Raleigh, C. B., and M. S. Paterson, Experimental deformation of serpentinite and its
788 tectonic implications, *J. Geophys. Res.*, *70*(16), 3965–3985, 1965.

- 789 Rudnicki, J. W., and J. R. Rice, Conditions for the localization of deformation in pressure-
790 sensitive dilatant materials, *J. Mech. Phys. Solids*, *23*, 371–394, 1975.
- 791 Rutter, E. H., and C. Glover, The deformation of porous sandstones; are Byerlee friction
792 and the critical state line equivalent?, *J. Struct. Geol.*, *44*, 129–140, 2012.
- 793 Rutter, E. H., S. Llana-Fùnez, and K. H. Brodie, Dehydration and deformation of intact
794 cylinders of serpentinite, *J. Struct. Geol.*, *31*, 29–43, doi:10.1016/j.jsg.2008.09.008, 2009.
- 795 Skarbek, R. M., and A. W. Rempel, Dehydration-induced porosity waves and episodic
796 tremor and slip, *Geochem. Geophys. Geosyst.*, *17*, doi:10.002/2015GC006155, 2016.
- 797 Smith, D. L., and B. Evans, Diffusional crack healing in quartz, *J. Geophys. Res.*, *89*(B6),
798 4125–4135, 1984.
- 799 Stefanou, I., and J. Sulem, Chemically induced compaction bands: Triggering conditions
800 and band thickness, *J. Geophys. Res.*, *119*(2), 880–899, 2014.
- 801 Sulem, J., and I. Stefanou, Thermal and chemical effects in shear and compaction bands,
802 *Geomech. Energy Environ.*, *6*, 4–21, 2016.
- 803 Tenthoery, E., and S. F. Cox, Reaction-enhanced permeability during serpentinite dehy-
804 dration, *Geology*, *31*(10), 921–924, 2003.
- 805 Wang, W. H., and T.-F. Wong, Effects of reaction kinetics and fluid drainage on the
806 development of pore pressure excess in a dehydrating system, *Tectonophysics*, *370*,
807 227–239, doi:10.1016/S0040-1951(03)00188-4, 2003.
- 808 Wilkinson, D. S., and M. F. Ashby, Pressure sintering by power law creep, *Acta Metall.*,
809 *23*, 1277–1285, 1975.
- 810 Wong, T.-F., and P. Baud, The brittle-ductile transition in porous rock: a review, *J.*
811 *Struct. Geol.*, *44*, 25–53, 2012.

⁸¹² Zhang, J., T.-F. Wong, and D. M. Davis, Micromechanics of pressure-induced grain crush-
⁸¹³ ing in porous rocks, *J. Geophys. Res.*, *95*(B1), 341–351, 1990.

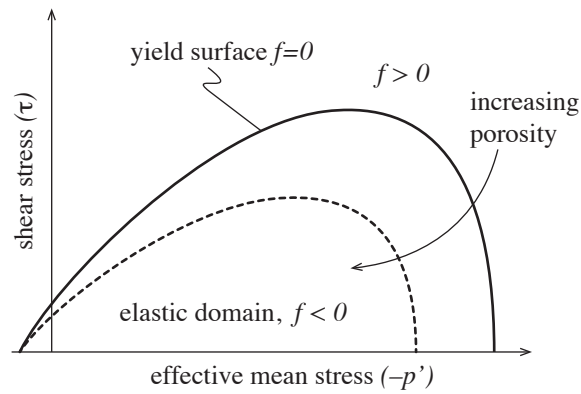


Figure 1. Schematic of the yield surface in the stress space (p', τ) . The yield surface is capped at elevated pressures, which corresponds to the possibility of yield under purely isotropic stress conditions. With increasing porosity, the yield surface tends to shrink (reducing the stress range for a purely elastic behaviour), as represented by the dashed line.

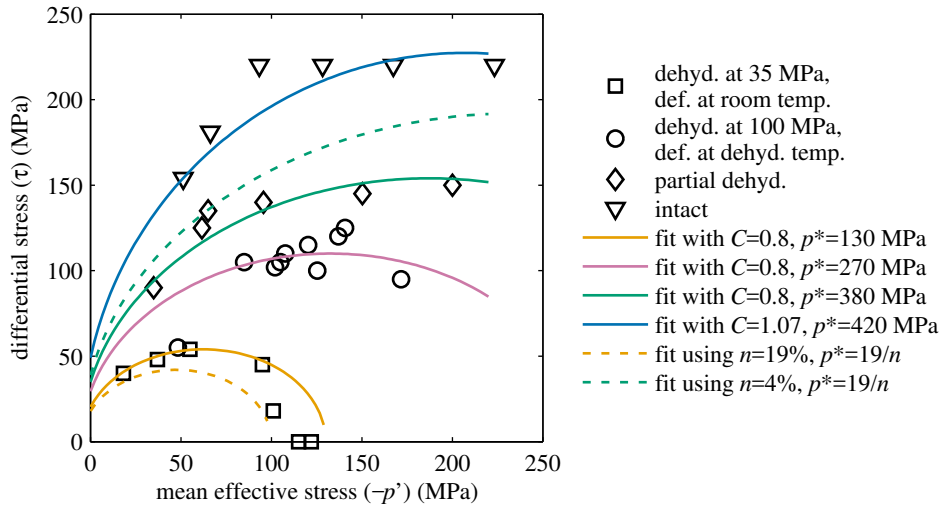


Figure 2. Yield surfaces of intact, partially and fully dehydrated serpentinites from *Rutter et al.* [2009], and fits with a modified Cam-clay model (equation 14). In all fits, we choose a tensile strength $b = 5$ MPa.

Table 1. Thermodynamic properties of phases involved in the dehydration reactions of antigorite. Data from *Holland and Powell* [1998].

	Molar weight	Molar volume	Thermal expansion	Bulk modulus	
	M	V_m°	α°	K°	$\partial K/\partial P$
Phase	g/mol	cm ³ /mol	$\times 10^{-5} \text{ K}^{-1}$	GPa	
Atg, antigorite	4536	1754.7	4.7	67.9	2.77
Talc	379.7	136.4	3.7	41.6	6.5
Fo, forsterite	140.7	43.7	6.1	127	5.37
Ens, enstatite	200.8	62.6	5.1	106	8.5
PhA, phase A	456.3	154.4	8.3	97.4	6.0

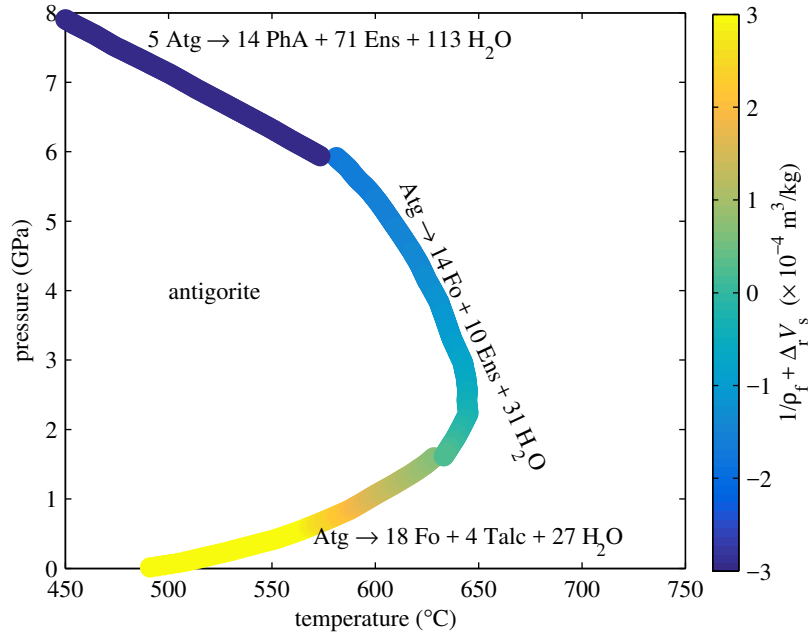


Figure 3. Net volume change $1/\rho_f + \Delta_r V_s$, in m^3 per unit mass of water, as a function of pressure and temperature, for each reaction. Atg: antigorite; Fo: forsterite; Ens: enstatite; PhA: phase A.

Table 2. Average fluid mass and volume change associated with the dehydration reactions of antigorite.

Reaction	Mass of releasable fluid	Volume change		
	m_d^0	$1/\rho_f + \Delta_r V_s$		
	(kg/m^3)	($\times 10^{-4} \text{ m}^3/\text{kg}$)		
		average	min.	max.
$\text{Atg} \rightarrow 4 \text{ Talc} + 18 \text{ Fo} + 27 \text{ H}_2\text{O}$	276	6.18	0.73	212.55
$\text{Atg} \rightarrow 14 \text{ Fo} + 10 \text{ Ens} + 31 \text{ H}_2\text{O}$	323	-1.02	-1.71	0.25
$5 \text{ Atg} \rightarrow 14 \text{ PhA} + 71 \text{ Ens} + 113 \text{ H}_2\text{O}$	240	-3.09	-3.22	-2.93

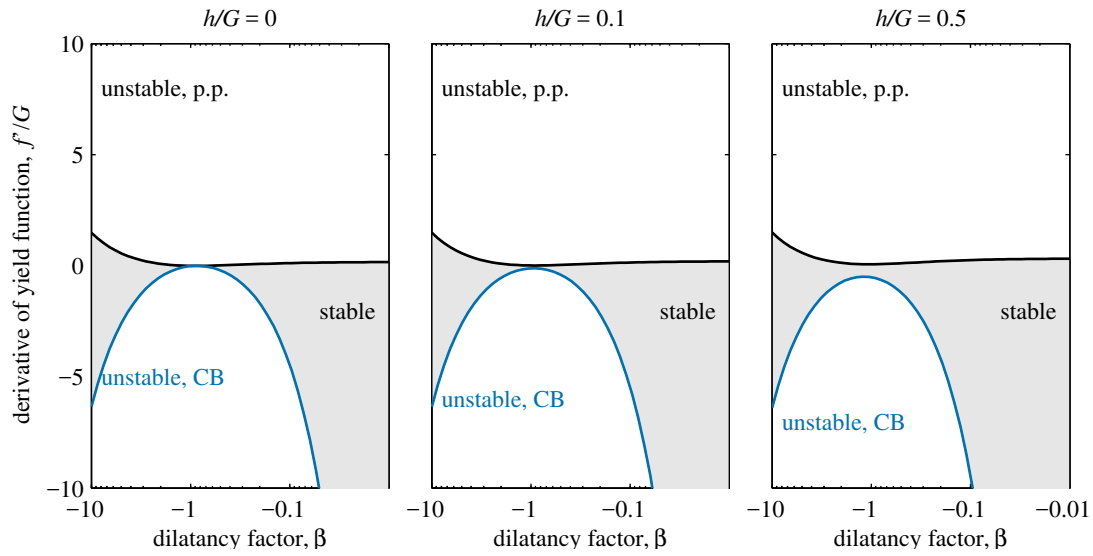


Figure 4. Stability boundaries for a dehydrating material with a porosity-dependent yield function. The dilatancy factor β has been assumed equal to the friction coefficient μ (i.e., we used the so-called associated plasticity assumption) in order to limit the number of free parameters. Black curves correspond to stability boundary for the pore pressure runaway (condition 30), and blue curves correspond to stability boundary for conventional (mechanical) compaction instability (condition 24).

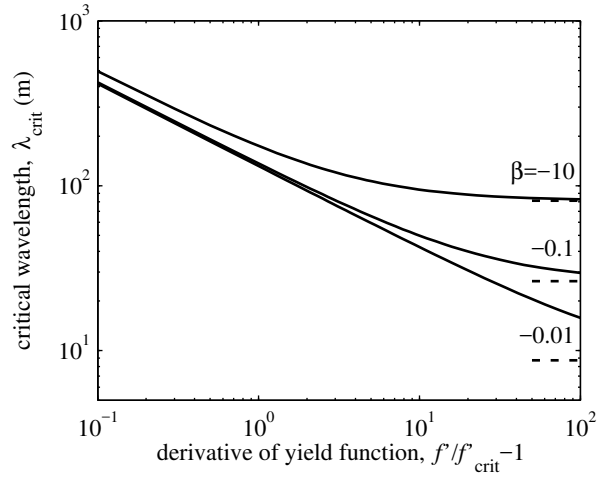


Figure 5. Critical unstable wavelength λ_{crit} . Values are reported in metres. The parameter values used here are those relevant to the dehydration of antigorite into enstatite and forsterite. For simplicity we assumed $h = 0$ and associated plasticity ($\beta = \mu$). The wavelength becomes infinite along the stability boundary, i.e., for f' approaching f'_{crit} , and approaches a constant (dashed lines) given by Equation (32) for $f' \gg f'_{\text{crit}}$.

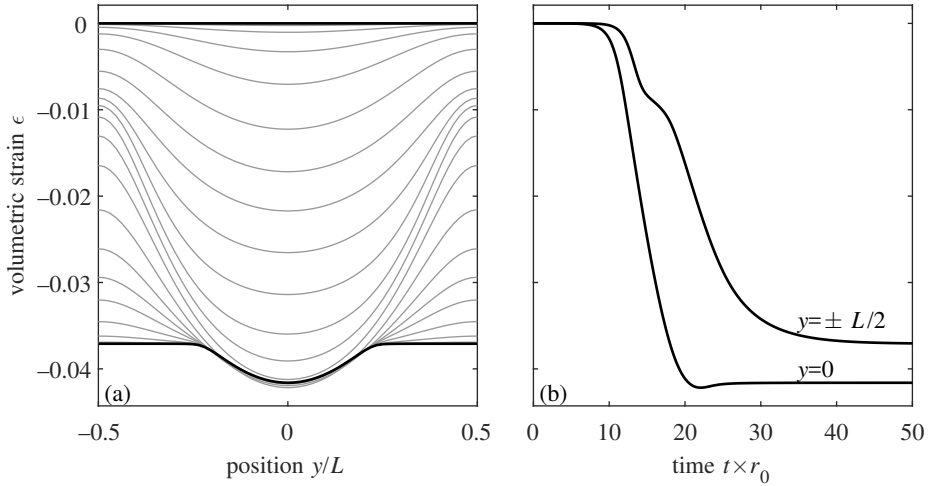


Figure 6. Nonlinear evolution of the compaction instability, modelled numerically. (a) Volumetric strain profiles as a function of time; initial and final profiles are shown in thick black lines, and intermediate profiles are in light grey. (b) Time evolution of volumetric strain at the centre ($y = 0$) and at the edges ($y = \pm L/2$) of the modelled layer.

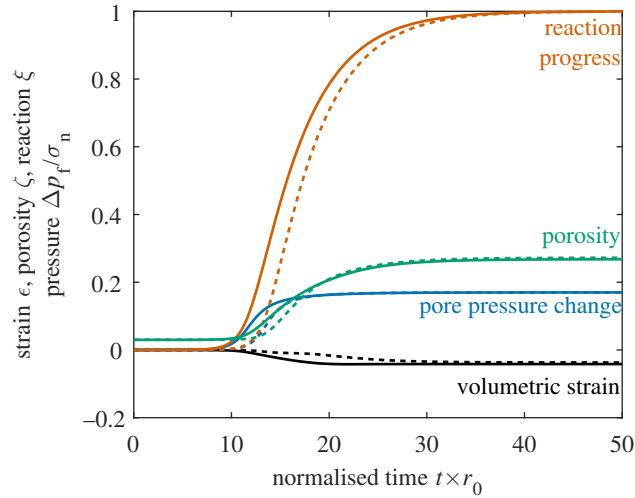


Figure 7. Volumetric strain ϵ (black), reaction progress ξ (orange), porosity ζ (green) and normalised pore pressure change $p_f - p_{f0}/\sigma_n$ (blue) as a function of normalised time $t \times r_0$. Solid lines show the evolution at the centre of the layer ($y = 0$), and dotted lines correspond to the evolution at the edge of the layer ($y = \pm L/2$).

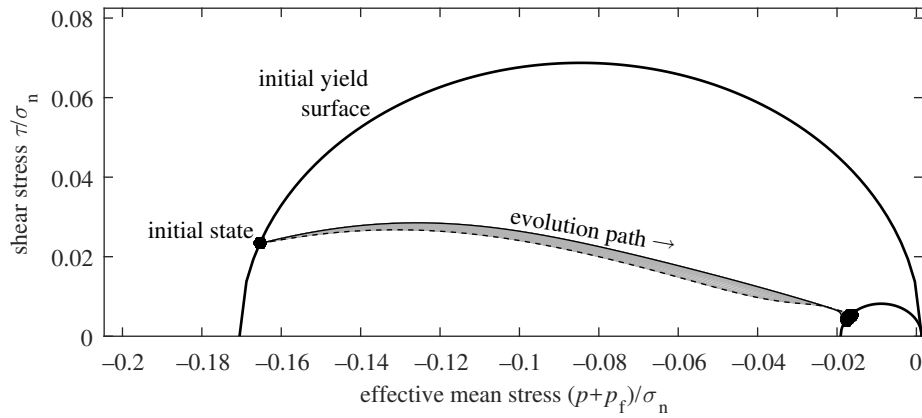


Figure 8. Stress path of material elements within the antigorite layer. The initial and final stress states are given by the filled black circles. The trajectory of the element in the centre of the layer is given by the solid black line, and that of the element at the edge is given by the dashed black line. The trajectories of all other elements are given as the thin grey lines. In this simulation, the total normal stress is $\sigma_n = 3.71$ GPa, so that the initial effective mean stress is 0.61 GPa and the initial shear stress is 0.09 GPa.